

# Fast and accurate circularization of a Rydberg atom

Sabrina Patsch,<sup>1</sup> Daniel M. Reich,<sup>1</sup> Jean-Michel Raimond,<sup>2</sup>  
Michel Brune,<sup>2</sup> Sébastien Gleyzes,<sup>2</sup> and Christiane P. Koch<sup>1</sup>

<sup>1</sup>*Theoretische Physik, Universität Kassel, Heinrich-Plett-Straße 40, D-34132 Kassel, Germany*

<sup>2</sup>*Laboratoire Kastler Brossel, Collège de France, CNRS, ENS-Université PSL, Sorbonne Université*

(Dated: March 29, 2018)

Preparation of a so-called circular state in a Rydberg atom where the projection of the electron angular momentum takes its maximum value is challenging due to the required amount of angular momentum transfer. Currently available protocols for circular state preparation are either accurate but slow or fast but error-prone. Here, we show how to use quantum optimal control theory to derive pulse shapes that realize fast and accurate circularization of a Rydberg atom. In particular, we present a theoretical proposal for optimized radio-frequency pulses that achieve high fidelity in the shortest possible time, given current experimental limitations on peak amplitudes and spectral bandwidth. We also discuss the fundamental quantum speed limit for circularization of a Rydberg atom, when lifting these constraints.

## I. INTRODUCTION

Circular Rydberg levels are quantum states of the valence electron that are characterized by a large principal quantum number and a maximum angular momentum projection [1]. They can be prepared by optical excitation of ground-state atoms into a low-angular-momentum Rydberg state, which is then exposed to a DC field, lifting the degeneracy of the Stark manifold, and to a near-resonant radio-frequency field, providing the required angular momentum [2].

Their long lifetime makes these states an ideal tool for applications in quantum technology. For example, they provide a key ingredient for microwave cavity quantum electrodynamics (CQED) [3], enabling the generation of non-classical states of a cavity mode [4]. Recently, they have attracted attention in the context of quantum interfaces [5] and quantum-enhanced sensing and metrology [6, 7]. In more detail, an electrometer with record sensitivity has been demonstrated using a superposition of two circular states in adjacent Stark manifolds of a rubidium Rydberg atom [6]. The repetition rate of the experiment is ultimately limited by the time required for the circular state preparation. Sensing of magnetic, instead of electric, fields, would be enabled by creating a coherent superposition of two circular states with opposite angular momentum projection quantum numbers. Both the electrometer and the magnetometer require the state preparation to proceed sufficiently fast to beat unavoidable decoherence.

Similarly, using Rydberg atoms to build an interface between optical and microwave photons [5] relies on fast coherent transfer between low- and high-angular-momentum states: While low-angular-momentum Rydberg states couple to optical photons and thus have short lifetimes, circular states do not. Circular states do, however, couple strongly to microwave photons. In other words, it is circularization from low- to high-angular-momentum states, together with its inverse process, that provides the link to interface optical and microwave pho-

tons. However, such an interface will work reliably only when the transfer proceeds both sufficiently fast and with high accuracy.

Fast coherent transfer to the circular state has recently been demonstrated by coupling a Rydberg atom to a radio-frequency (RF) field with a well-defined polarisation [2]. The near-resonant RF drive implements a Rabi oscillation between a low-angular-momentum state and the circular one, which allows the circularization to proceed in about 200 ns. However, the transfer rate was limited to about 80% by the anharmonicity of the Stark manifold and perturbations due to the finite quantum defects of the low-angular-momentum states [2]. Another possibility to perform the circularization is rapid adiabatic passage [1, 8], which relies on the slow transformation of instantaneous eigenstates using chirped RF pulses or slow variations of the DC field. Here, fidelities close to 100% are achievable, but the required time is much longer, namely several microseconds. As a result, large dynamic phases are accumulated which are error-prone due to imperfections in the control. These errors propagate in the microwave-to-optical interface or when generating a coherent superposition of opposite angular momentum states. This problem of adiabatic passage is generic; it is also encountered, for example, when utilizing stimulated Raman adiabatic passage (STIRAP) to realize quantum gates in Rydberg atoms: While population can be transferred very efficiently, precise control over the phase is extremely difficult and the famous robustness of STIRAP is lost [9]. In the context of quantum-enhanced sensing and metrology or quantum interfaces, adiabatic passage thus does not provide a viable route.

Further improvement of the coherent transfer protocol of Ref. [2] is hampered by the complexity of the dynamics that proceeds in a comparatively large Hilbert space. Fast and accurate preparation of a circular Rydberg state thus remains an open challenge. Here, we show how to use quantum optimal control theory to tackle this problem.

Quantum optimal control theory is based on defining

a figure of merit, here the state preparation fidelity, and treating it as a functional of the external controls. The latter are then determined using e.g. variational calculus [10]. The control problem is most often solved numerically, and large Hilbert spaces do not pose a problem as long as the time evolution of the system can be calculated with reasonable numerical resources. Quantum optimal control theory is an ideal tool whenever high fidelity is desired [10]. Being biased against adiabatic solutions [11], it is, moreover, well suited to identify protocols that require the minimum amount of time for a given process [12]. For example, quantum optimal control theory has been used to determine the shortest time required for transport in a spin chain [12] and the fastest universal set of gates within circuit QED [13].

The paper is organized as follows. Section II introduces our model to describe the Rydberg atom, whereas quantum optimal control theory is briefly reviewed in Sec. III. Section IV explains how, based on a thorough understanding of the circularization dynamics exploited in Ref. [2], a guess pulse is constructed that, when optimized, provides the desired fast and accurate transfer while obeying current experimental constraints. The robustness of our control solution is analyzed for various noise sources in Sec. V. Finally, Sec. VI explores how far the quantum speed limit can be pushed when lifting typical experimental constraints, and Sec. VII concludes.

## II. MODEL

We consider the single valence electron of an alkali atom. Without an external field, the energy spectrum is given by the quantum defect theory [14]. Briefly, a complete set of quantum numbers consists of the principal, orbital angular momentum, and projected angular momentum quantum numbers,  $n$ ,  $\ell$  and  $m_\ell$ , similarly to the hydrogen atom. Imperfect shielding of the nuclear charge by the core electrons breaks the degeneracy of the eigenenergies for small  $\ell$ , when the valence electron is close to the nucleus. The corresponding quantum defect is accounted for by a correction  $\delta_{n\ell j}$  to the Rydberg formula for the eigenenergies [15]

$$E_{n\ell j} = -\frac{1}{2(n - \delta_{n\ell j})^2}, \quad (1)$$

where atomic units ( $\hbar = 1$ ) are employed throughout and  $j$  is the total angular momentum quantum number,  $|\ell - s| \leq j \leq \ell + s$ . Since the quantum defect does not break the spherical symmetry,  $n$ ,  $\ell$ , and  $m_\ell$  are still good quantum numbers. In our calculations, we use a perturbative expansion of  $\delta_{n\ell j}$  up to second order. We use the values given in Ref. [16], corresponding to rubidium 85 for  $n \geq 20$ . The quantum defect is neglected for states with  $\ell > 7$  and we neglect spin-orbit coupling. Because the quantum defect is  $j$ -dependent, we choose  $j = \ell + s = \ell + \frac{1}{2}$  throughout.

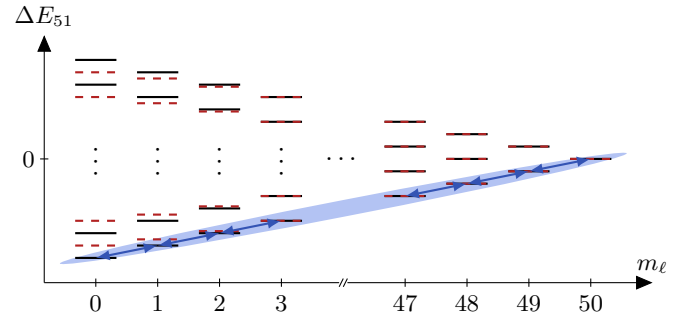


FIG. 1. Schematic spectrum for  $m_\ell \geq 0$  of the  $n = 51$ -manifold for hydrogen (black) and rubidium (dashed red) with a moderate DC field. The zero of energy was set to the field-free position of the manifold. The states of rubidium with  $|m_\ell| \leq 2$  are significantly affected by the quantum defect. The blue ellipse indicates the lowest diagonal ladder whose states are connected by  $\sigma^+$ -polarized transitions (blue arrows).

In the presence of a DC electric field, the spherical symmetry is broken and  $\ell$  is not a good quantum number anymore. However, the component of the angular momentum along the direction of the DC field is conserved such that  $m_\ell$  is still a good quantum number. Incidentally, neglecting the quantum defect (i.e. considering a hydrogen atom), the projection of the Runge-Lenz vector along the direction of the DC field is also conserved. This gives rise to the eccentricity quantum number  $\mu$ , which, for given  $n$  and  $m_\ell$ , takes the values  $-(n - |m_\ell| - 1)$ ,  $-(n - |m_\ell| - 1) + 2, \dots, (n - |m_\ell| - 1) - 2, (n - |m_\ell| - 1)$ . Note that  $\mu$  alternates between only odd and only even numbers for different values of  $m_\ell$ . Perturbation theory in first and second order yields the DC Stark shifts [17],

$$\Delta E^{(1)} = \frac{3}{2} \mu n \mathcal{E}_{\text{DC}}, \quad (2a)$$

$$\Delta E^{(2)} = -\frac{1}{16} n^4 (17n^2 - 3\mu^2 - 9m_\ell^2 + 19) \mathcal{E}_{\text{DC}}^2, \quad (2b)$$

where  $\mathcal{E}_{\text{DC}}$  denotes the DC field strength, which is taken to be of the order of 1 V/cm. For such moderate DC field strengths, the second-order Stark effect can be neglected and the eigenvalues form ladders for fixed  $n$  and  $m_\ell$  (cf. black energy levels in Fig. 1). The ladders with  $\pm m_\ell$  are identical, and neighboring ladders,  $\Delta m_\ell = \pm 1$ , have an energy offset of half a ladder step. The number of steps in each ladder is given by  $n - |m_\ell|$ .

An RF field, perpendicular to the DC one, induces transitions between neighboring ladders. Pulses with a  $\sigma^+$  polarization drive transitions between states with  $\Delta m_\ell = +1$  whilst increasing the energy, whereas transitions between states with  $\Delta m_\ell = -1$  are accompanied by a decrease in energy. The opposite rules apply for  $\sigma^-$ -polarized pulses. The states where the magnetic and the eccentricity quantum number change by one lie on so-called diagonal ladders. In the following, we will only consider the lowest diagonal on the right hand side of

the manifold, with  $m_\ell \geq 0$ . Its states are connected by  $\sigma^+$ -polarized transitions (cf. blue ellipse and arrows in Fig. 1). Due to the harmonicity within the Stark manifold, the states on this diagonal ladder can be interpreted as the  $|J, M\rangle$  states of a large spin- $J$  system with  $J = (n-1)/2$  and  $M = m - J$  [6]. The energy levels are pairwise separated by  $\omega_{\text{at}}$ , which is given by the first order Stark shift (cf. Eq. (2a)) and of the order of 100 MHz for  $\mathcal{E}_{\text{DC}} = 1$  V/cm and  $n \approx 50$ . In this analogy, the circular state corresponds to the North pole  $|J, M = J\rangle$  of the generalized Bloch sphere. The coordinates  $(X, Y, Z)$  of the Bloch vector on the sphere are given by the expectation values of the  $x$ -,  $y$ - and  $z$ -component of the angular momentum vector  $\vec{J}$ , respectively. In these terms, applying a  $\sigma^+$ -polarised pulse with phase  $\phi_{\text{RF}} = \varphi + \pi/2$  and detuning  $\delta = \omega_{\text{at}} - \omega_{\text{RF}}$  leads to a rotation of the Bloch vector along

$$\vec{\Omega} = (-\Omega_R \sin \varphi, \Omega_R \cos \varphi, \delta) \quad (3)$$

with the Rabi frequency

$$\Omega_R = 3 \mathcal{E}_{\text{RF}} n, \quad (4)$$

where  $\mathcal{E}_{\text{RF}}$  is the amplitude of the RF field. In the resonant case,  $\delta = 0$ , and when starting from the circular state, the RF field induces a rotation to the  $(\vartheta, \varphi)$ -direction where  $\vartheta = \Omega_R T$ . The resulting state,  $|\vartheta, \varphi\rangle$ , is called a spin coherent state (SCS) in analogy to the coherent states in quantum optics [18].

When alkali atoms are considered, the quantum defects perturb the harmonicity of the Stark manifold (cf. red energy levels in Fig. 1). For small values of  $|m_\ell|$ , states can be missing from the manifold if the energy shift due to their quantum defect is much larger than their Stark shift. For the DC fields considered here, states are missing in vertical ladders with  $|m_\ell| \leq 2$ . This results in irregular offsets of the vertical ladders and anharmonic diagonal ladders. This can be seen from the blue arrows on the left hand side in Fig. 1, which are detuned from the transitions between the red energy levels. For  $|m_\ell| = 2$ , only a single state is missing, and the harmonicity of the lowest diagonal ladder towards higher values of  $m_\ell$  is almost preserved, while it is broken towards the other side. This makes the lowest level of the  $|m_\ell| = 2$  ladder the ideal starting point for circularization [16], i.e., for the transition to the circular state with  $m_\ell = n - 1$  and  $\mu = 0$ .

To optimize the electron's dynamics in the circularization process, we need to numerically compute the Hamiltonian. Thus, we have to calculate the matrix elements of the interaction Hamiltonian,  $V = -\vec{d} \cdot \vec{\mathcal{E}}$ , where  $\vec{d} = q\vec{r}$  denotes the dipole operator and  $\vec{\mathcal{E}}$  is either the DC or RF electric field,  $\vec{\mathcal{E}}_{\text{DC}}$  or  $\vec{\mathcal{E}}_{\text{RF}}(t)$ . To this end, the matrix elements are split into their radial and angular parts. The latter can be expressed in terms of the Clebsch-Gordan coefficients [19]. The radial part is calculated numerically, using Numerov's method [20].

To speed-up the numerical calculations during the propagation and optimization, the total Hilbert space has to be reduced. For this purpose, we only take into account states that have a large dipole matrix element with at least one of the 'pivotal' states on the lowest diagonal ladder. As it turns out, it is sufficient to take the lowest and second lowest diagonal ladders into account during the calculations. However, all calculations were cross-checked by comparing to calculations with a Hamiltonian defined on a larger Hilbert space that contains all states of the  $n$ -manifold.

Finally, the time-dependent Schrödinger equation,

$$i\hbar \frac{\partial}{\partial t} |\psi(t)\rangle = H(t) |\psi(t)\rangle, \quad (5)$$

is solved numerically with the Chebychev propagator [21], using the qdyn library [22]. In the numerical implementation, the  $|\psi(t)\rangle$  state is expanded in the eigenbasis of the Stark states in the presence of the DC field. The time-dependence in the Hamiltonian arises from the time-dependence of the RF field strength,  $\vec{\mathcal{E}}_{\text{RF}}(t)$ .

### III. OPTIMAL CONTROL THEORY

The goal of this work is to drive the population from the initial state  $|\Psi(0)\rangle$  towards the target circular state  $|\Psi_{\text{tgt}}\rangle$  as fast and as accurately as possible. To this end, we employ quantum optimal control theory (OCT) [10, 23]. The success of the desired state-to-state transfer can be quantified by the following 'cost' functional [24],

$$J_T = 1 - |\langle \Psi(T) | \Psi_{\text{tgt}} \rangle|^2. \quad (6)$$

It depends implicitly on the set of external control fields  $\{\mathcal{E}_k\}$  via the final state  $|\Psi(T)\rangle$ , where  $k$  labels the different control fields. To limit the pulse amplitude or to avoid lossy regions of Hilbert space, one can impose additional constraints  $g[\{\mathcal{E}_k\}, \{|\psi_j(t)\rangle\}]$  to the fields and to the states at intermediate times  $\{|\psi_j(t)\rangle\}$ , where  $j$  runs over the basis states [24, 25],

$$J[\{|\psi_j\rangle\}, \{\mathcal{E}_k\}] = J_T + \int_0^T dt g[\{\mathcal{E}_k\}, \{|\psi_j(t)\rangle\}]. \quad (7)$$

Here, we seek to minimise the required field amplitude and restrict ourselves to one control field,  $\vec{\mathcal{E}}_{\text{RF}}(t) = \mathcal{E}_{\text{RF}}^x(t) \vec{e}_x + \mathcal{E}_{\text{RF}}^y(t) \vec{e}_y$ , where the  $x$ - and  $y$ -component are optimized independently from each other. Consequently, even when we start with a  $\sigma^+$ -polarized guess pulse, the polarisation is not necessarily conserved in the optimized field. Then, the constraints in Eq. (7) can be chosen as [24]

$$g[\vec{\mathcal{E}}_{\text{RF}}] = \frac{\lambda}{S(t)} \left( \vec{\mathcal{E}}_{\text{RF}}(t) - \vec{\mathcal{E}}_{\text{ref}}(t) \right)^2, \quad (8)$$

with  $S(t) \in [0, 1]$  being a shape-function to smoothly switch the field on and off, and  $\lambda$  being a weight. The

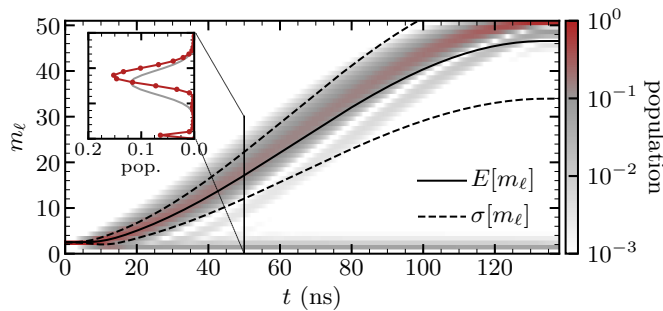


FIG. 2. Distribution of the population over the lowest diagonal ladder for a  $\pi$ -pulse as described in Sec. IV A. Note the logarithmic scale in the color bar. The expectation value  $E[m_\ell]$  and the standard deviation  $\sigma[m_\ell]$  are indicated by the solid and dashed lines, respectively. The large variance is caused by the non-negligible population in  $m_\ell = 1$ . The inset displays the population distribution at  $t = 50$  ns for  $m_\ell \leq 30$ . The grey line shows the population distribution of the closest SCS  $|\psi_{\text{SCS}}^{(\vartheta=0.62\pi, \varphi=0.49\pi)}\rangle$ .

reference field  $\vec{\mathcal{E}}_{\text{ref}}(t)$  is usually the pulse from the previous iteration [23, 24]. In the following, we use Krotov's method [26] in its adaption to quantum dynamics [23, 24, 27, 28] to carry out the optimization. It consists in a sequential, gradient-based algorithm, which proceeds by forward propagation of the initial state and backwards propagation of the target state, followed by an update of the field in order to match the two. The specific update formula used here is found e.g. in Refs. [23, 24].

#### IV. FAST CIRCULARIZATION WITH CONSTRAINED AMPLITUDE AND BANDWIDTH

We refer to circularization as transfer from the lowest lying state of the  $m_\ell = 2$ -ladder to the circular state. This 'initial' state has to be prepared beforehand, starting with a rubidium atom in the ground  $5S_{1/2}$  state [2]. To this end, the rubidium atoms are optically excited using three laser fields in the presence of a weak DC field [6]. The target state of the optical excitation,  $|51f, 2\rangle$ , can be precisely addressed due to its weak quantum defect. Afterwards, the DC field is slowly increased to its final value. This enlarges the spacing of the states in the Stark manifold, and the state  $|51f, 2\rangle$  becomes adiabatically the lowest lying state of the  $m_\ell = 2$ -ladder. Now, the actual circularization can take place, where the circular state is reached via an  $n$ -level Rabi oscillation.

##### A. $\pi$ -pulse

As a first guess for the optimization, we choose an RF  $\pi$ -pulse driving  $\sigma^+$ -transitions within the lowest diagonal ladder of the manifold. This pulse represents the present

state of the art in the experiment [2, 16]. Due to the quantum defect, this pulse is near-resonant with transitions to the right side of the initial state, whereas it is slightly detuned from the transition to the left side (cf. Fig. 1). Because only states in the lowest diagonal ladder play a significant role during the circularization, we will denote these states by  $|m_\ell\rangle$  for the sake of simplicity. The initial state becomes  $|2\rangle$  and the target circular state  $|50\rangle$ .

Following Ref. [16], we choose the  $n = 51$ -manifold and  $\mathcal{E}_{\text{DC}} = 2.346$  V/cm. The quasi-resonant frequency of the ladder is  $\omega_0 = 229.6$  MHz, which has been calculated using the first-order Stark splitting of hydrogen (cf. Eq. (2a)). The chosen guess pulse is a  $\sigma^+$ -polarized RF pulse with central frequency  $\omega_{\text{RF}} = 230$  MHz and amplitude  $\mathcal{E}_{\text{RF}} = 18$  mV/cm. The pulse has a flat-top shape with sine-squared edges lasting 10 ns each. The total duration of the pulse,  $t_{\text{stop}} = 138$  ns, has been adjusted to match a  $\pi$ -pulse.

The final population in the circular state is 81% with an expectation value of  $m_\ell$  equal to 46. This indicates that the population is spread over several ladder states, as can be seen in Fig. 2. A large fraction of the missing population (6% of the total population) can be found in the state  $|1\rangle$ . This effect can be attributed to an insufficient detuning of the RF pulse from the  $|2\rangle \rightarrow |1\rangle$  transition. The transition frequencies  $\omega_{m_\ell, m'_\ell} \equiv E_{|m'_\ell\rangle} - E_{|m_\ell\rangle}$  between the relevant states are

$$\omega_{0,1} = 70.36 \text{ MHz}, \quad (9a)$$

$$\omega_{1,2} = 182.95 \text{ MHz}, \quad (9b)$$

$$\omega_{2,3} = 227.46 \text{ MHz}. \quad (9c)$$

The quantum defect barely affects the  $m_\ell = 2$ -ladder and  $\omega_{2,3}$  is nearly resonant with the RF pulse, while the detuning from  $\omega_{0,1}$  is large enough to prevent a significant population of state  $|0\rangle$ . However, the rather small detuning from  $\omega_{1,2}$  allows for an off-resonant drive towards state  $|1\rangle$ . While some of this population remains trapped in state  $|1\rangle$ , another part is reflected from the lower bound of the ladder and follows the main packet towards the circular state with a small delay. This can be seen from the light grey streak slightly below the main red path and from the strong deviation of the expectation value of  $m_\ell$  from the center of the population distribution in Fig. 2.

Moreover, the inset in Fig. 2 displays the population distribution at the intermediate time,  $t = 50$  ns, together with the closest SCS  $|\psi_{\text{SCS}}^{(\vartheta=0.62\pi, \varphi=0.49\pi)}\rangle$ . The latter is the SCS with coordinates that best match the expectation values of the three spatial components of the angular momentum vector for the system state  $|\psi(t = 50 \text{ ns})\rangle$  (cf. Sec. II). Apparently, the upper peak of  $|\psi(t = 50 \text{ ns})\rangle$  is more narrow than a SCS and the residual population in the low- $m_\ell$  states affects the position of  $|\psi_{\text{SCS}}^{(\vartheta, \varphi)}\rangle$  on the  $m_\ell$ -axis significantly. Thus, the overlap of  $|\psi_{\text{SCS}}^{(\vartheta=0.62\pi, \varphi=0.49\pi)}\rangle$  and  $|\psi(t = 50 \text{ ns})\rangle$  is only 65%. As explained in Sec. II, a SCS can be rotated into the target

circular state in a very natural way. However, due to the deviation from a perfect SCS, part of the population at the final time is spread over several states neighboring the target.

To summarize our observations from Fig. 2, the fidelity obtained with a  $\pi$ -pulse is limited by (i) loss to  $|1\rangle$ , (ii) delay due to reflection from the lower end of the ladder, and (iii) an imperfectly-shaped SCS. These effects together result in an infidelity of about 19% at the final time. One could now directly use the  $\pi$ -pulse as a guess field to start the optimization, which provides an optimized pulse leading to a fidelity of 99%. However, such a brute force approach comes at the expense of rather complex optimized fields with an undesirably large spectral bandwidth and a high field strength. In view of the experimental feasibility of the optimized pulse, it is much more advantageous to first exploit the available physical insight and construct an improved guess pulse before starting the optimization.

### B. Two-step amplitude guess pulse

The observations above suggest to split the circularization into the preparation of a SCS and a subsequent rotation of the SCS into the target state. Before constructing a pulse that implements such a two-step circularization, let us first estimate the maximal speed up of the circularization that can be expected.

As with any dynamics on the Bloch sphere, the fastest rotation is obtained when the maximum allowed field amplitude is used. We choose  $\mathcal{E}_{\text{RF}} = 45 \text{ mV/cm}$ , which is close to the maximal, experimentally feasible value,  $\frac{\Omega_R}{2\pi} = 9 \text{ MHz}$  or  $\mathcal{E}_{\text{RF}} \simeq 46 \text{ mV/cm}$ , cf. Eq. (4). Numerically, we find the optimal duration of the pulse to be 61.2 ns (data not shown), which is slightly faster than the analytical prediction for a  $\pi$ -pulse, which is 66.9 ns. The difference is explained by the fact that the initial state,  $|2\rangle$ , does not coincide with the South pole of the Bloch sphere. Instead, it corresponds to a ring on the Bloch sphere around the  $Z$ -axis with  $Z \approx -0.9$  (the radius of the sphere being normalized to 1).

While this amplified  $\pi$ -pulse is more than twice as fast as the one in the previous section, its fidelity is decreased to 63%. Obviously, for larger field strengths, the non-resonant run-off of population becomes more significant. In addition to the 61.2 ns for the mere rotation of a SCS, the accurate preparation of the SCS itself needs some time. Therefore, the approach to obtain high fidelity with the shortest possible duration is to increase the pulse duration gradually until the desired fidelity of  $J_T = 10^{-2}$  can be reached under given constraints. Note that higher fidelities could easily be realized in the calculations. However, this will not be meaningful in view of application in an experiment where detector efficiency, DC electric field inhomogeneities, electric field noise and other experimental imperfections [6] intrinsically limit the measurable fidelity. The lengthening of the pulse is motivated by the

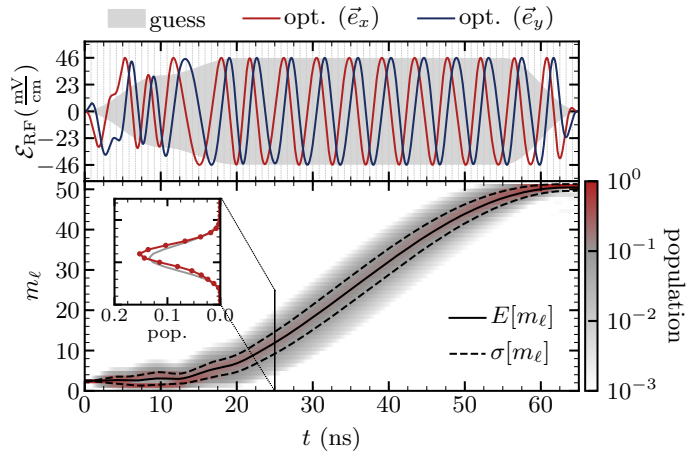


FIG. 3. Top: Guess pulse (grey shape) and optimized pulse (red and blue lines corresponding to the  $x$ - and  $y$ -component of the pulse, respectively). The dashed grid lines depict the step size of the coarse graining of the AWG (0.83 ns). Bottom: Same as Fig. 2 but for the optimized pulse leading to a fidelity of 99%. The grey line shows the population distribution of the closest SCS  $|\psi_{\text{SCS}}^{(\vartheta=0.69\pi, \varphi=0.54\pi)}\rangle$ .

necessity to reduce the amplitude in the beginning of the circularization, in order to avoid population running off to the state  $|1\rangle$  and allowing sufficient time for the preparation of the SCS.

It turns out that the shortest possible pulse, cf. top panel of Fig. 3 (grey shape), has a duration of 65 ns. Its initial amplitude has been decreased to 30 mV/cm. After 10 ns the amplitude is increased to the maximum value, 45 mV/cm. This increase takes another 10 ns and uses a sine-squared shape. The edges of the pulse are unchanged. The new guess pulse, referred to as two-step amplitude pulse, leads to a fidelity of 74%, which is already a significant gain compared to the simple 61.2 ns  $\pi$ -pulse. Notably, the final population in state  $|1\rangle$  under the new guess pulse is decreased to only  $6 \times 10^{-6}$ .

### C. Optimization results

Next, we seek to increase the fidelity of the two-step amplitude pulse by employing Krotov's method (cf. Sec. III). The optimization is performed until the functional crosses the threshold  $J_T = 10^{-2}$ , which corresponds to a fidelity of 99%. The considered shape function  $S(t)$  (cf. Eq. (8)) is the previously described sine-squared function. To ensure experimental feasibility, the absolute value of the amplitude is constrained to values smaller than 46 mV/cm. Spectral components driving either  $\sigma^-$ -polarized or  $\sigma^+$ -polarized transitions above 460 MHz are suppressed. This is most simply achieved by cutting the amplitude and spectrum of the pulse to the allowed range after each iteration. While such a procedure typically results in loss of monotonic convergence of



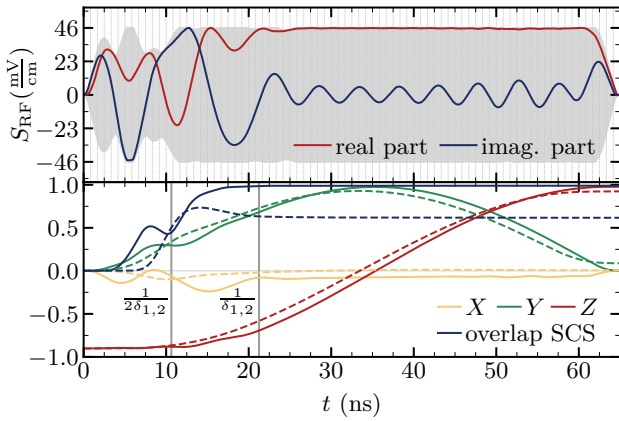


FIG. 4. Top: Complex shape function of the optimized pulse. The pulse is separated in its real (red) and imaginary (blue) part while the envelope is represented by the grey shade in the background. The dashed grid lines in the background depict the step size of the coarse graining (0.83 ns). Bottom: Temporal evolution of the Bloch vector coordinates  $X$ ,  $Y$  and  $Z$  in a frame rotating with  $\omega_{\text{RF}}$  and of the overlap of the propagated state with the closest SCS  $|\psi_{\text{SCS}}^{(\vartheta, \varphi)}\rangle$ . Shown are the dynamics driven by the guess pulse (dashed lines) and optimized pulse (solid lines). The vertical lines show the time scale of the detuned  $|2\rangle \rightarrow |1\rangle$  transition.

the optimization [29–31], in our case  $J_T$  does converge monotonically due to the high quality of the guess pulse. All in all, 1390 iterations were needed to cross the threshold. One iteration requires a computation time of  $\sim 50$  s on a standard work-station for the considered part of the manifold (the two lowest diagonal ladders with  $m_\ell \geq 0$ ).

Comparison of the guess and optimized pulse, cf. top panel of Fig. 3, reveals that the pulse is mainly changed in the low-amplitude step while it is left nearly unaltered in the high-amplitude step except for a shortening of the edge time. The shorter edge times and the stronger time dependence in the beginning of the pulse lead to a broadening of the spectrum but no conspicuous resonances appear in the spectrum other than the near-resonant transitions at 230 MHz.

Inspection of the population dynamics under the optimized pulse, cf. bottom panel of Fig. 3, reveals that the population is focused onto a few states with a small standard deviation and without any significant population remaining in the low- $m_\ell$  states. Moreover, it confirms the already predicted evolution: In the beginning, a SCS is generated, which is then driven towards the target state easily. As can be seen in the inset, the state at  $t = 25$  ns is very close to an SCS. Indeed, its overlap with the closest SCS  $|\psi_{\text{SCS}}^{(\vartheta=0.69\pi, \varphi=0.54\pi)}\rangle$  indicated by the grey line is 98.9%.

A deeper understanding of the dynamics is most easily gained when the process is considered in a frame rotating with  $\omega_{\text{RF}}$ . Accordingly, we demodulate the optimized pulse with the carrier frequency  $\omega_{\text{RF}}$ . The result is a

complex envelope  $S_{\text{RF}}(t)$  such that

$$\begin{aligned} \vec{\mathcal{E}}_{\text{RF}}(t) = & \text{Re}(S_{\text{RF}}(t)) (\cos(\omega_{\text{RF}}t)\vec{e}_x + \sin(\omega_{\text{RF}}t)\vec{e}_y) \\ & + \text{Im}(S_{\text{RF}}(t)) (-\sin(\omega_{\text{RF}}t)\vec{e}_x + \cos(\omega_{\text{RF}}t)\vec{e}_y), \end{aligned} \quad (10)$$

see also top panel of Fig. 4. The real part of the envelope can be interpreted as the shape of an RF pulse with phase  $\phi_{\text{RF}} = 0$  (called the first quadrature), which induces a rotation around the  $x$ -axis of the generalized Bloch sphere (cf. Eq. (3)). Conversely, the imaginary part corresponds to the shape of a pulse that is phase-shifted by  $\pi/2$  (called the second quadrature), which induces a rotation around the  $y$ -axis. The first quadrature is the dominating one as can be seen from the red curve coinciding with the envelope of the pulse for most of the time.

The role of the two quadratures becomes evident when considering the evolution of the state on the Bloch sphere, cf. bottom panel of Fig. 4. It is constructive to consider the evolution driven by the guess pulse first (dashed lines). The guess pulse consists of the first quadrature only, which induces a rotation around the  $x$ -axis. Since the initial state corresponds to a ring around the  $z$ -axis on the Bloch sphere, population with positive  $Y$ -components is rotated to higher  $Z$ -values whereas population with negative  $Y$ -components is rotated towards  $|1\rangle$ . This off-resonant transition needs  $1/(2\delta_{1,2}) = 10.6$  ns, which is additionally accompanied by a rotation around the  $z$ -axis (cf.  $z$ -component of  $\vec{\Omega}$  in Eq. (3)). Because the rotation only affects part of the state, the cylindrical symmetry of the initial state is broken. This can be seen from the dip in the  $X$ -component at 10.6 ns. The accumulated population in  $|1\rangle$  then oscillates back towards  $|2\rangle$  at  $1/\delta_{1,2} = 21.2$  ns. Afterwards, the shape of the state does not change anymore (as can be seen from the constant overlap with a SCS) and the  $X$ -component is increasing only a little due to the second-order Stark shift. While, at the final time, the values of  $X$ ,  $Y$  and  $Z$  are close to the target, the inaccurate shape of the state due to the dynamics in the first approximately 20 ns is the main cause of the insufficient final fidelity.

Thus, the main task of the optimized pulse is to improve the shape of the state. It is evident from Fig. 4 that the first 21 ns of the pulse are designated to generate the required high-fidelity SCS. When the initial state splits in the very beginning, as explained above, both quadratures contribute to a clear separation of the two parts. This can be seen in Fig. 3 from the partitioning of the population into two distinct branches around 10 ns. In particular, the part with  $m_\ell > 2$  is brought to a SCS-like shape much earlier, at 8 ns, than for the guess pulse (cf. peak in the overlap of the state with a SCS in Fig. 4). The  $X$ -value goes to zero here because the SCS-like state is located exactly opposite of the remaining population in  $|1\rangle$ . When the population that has been driven to  $|1\rangle$  joins the SCS-like state, the overlap decreases a bit before reaching its maximal value of 99% after 21.2 ns, in agreement with the time scale of the off-resonant oscillation to  $|1\rangle$ . Note that the remaining inaccuracy is retained until

the end and is the main cause of the final error of 1%.

The polar angle of the closest SCS  $|\psi_{\text{SCS}}^{(\vartheta, \varphi)}\rangle$  amounts to  $\vartheta = 0.75\pi$ . The time that is required to rotate this state towards the North pole with the maximally allowed field strength is given by  $T = \vartheta/\Omega_R = 42\text{ ns}$ . This rotation is visible in Fig. 4 by the smoothly increasing  $Z$ -component and the flat shape of the first quadrature. At the same time, the second quadrature helps to adjust the  $X$ -component of the state to compensate for the drift due to the second-order Stark effect. The peak of the second quadrature at  $62.5\text{ ns}$  induces a final adjustment of the  $X$ -component and kicks the SCS to the circular state. Finally, by adding a small overhead due to the edges of the pulse, the calculated time scales are in full agreement with the duration of the numerically determined time-optimal pulse.

To corroborate our finding on “time-optimality”, we have tested several values for initial and final pulse amplitude, duration and start of the amplitude ramp. It turns out that the crucial parameter for the success of the optimization under the given constraints is the pulse duration. This confirms the discussion of the previous paragraph. In fact, several different guess pulses with the same duration lead to almost the same optimized pulse. Pulses which are longer than  $65\text{ ns}$  can also be optimized to the desired fidelity within a similar number of iterations (of the order of 2000). On the other hand, no shorter pulse (such as the  $61.2\text{ ns}$  pulse described above) can be optimized to the desired fidelity under the given constraints within at least  $10^4$  iterations.

## V. ROBUSTNESS AGAINST NOISE

To estimate the performance of our theoretical predictions under experimental conditions, we investigate the stability of the optimized two-step amplitude pulse with respect to different sources of noise.

### A. Coarse graining

In an experiment, the optimized pulse is realized by an arbitrary waveform generator (AWG), which samples the pulse at discrete points in time. The AWG is limited to a frequency bandwidth of  $480\text{ MHz}$  for two channels. This constraint is fulfilled by the optimized pulse due to the bandwidth restriction during the optimization. In addition, the maximum sampling rate of  $1.2\text{ GS/s}$  leads to a temporal step size of  $0.83\text{ ns}$ . This limitation might have a severe impact on the fidelity.

To examine the influence of the limited resolution, we perform a coarse graining of the optimized pulse. In between two time steps, the pulse shape is interpolated linearly. This is a reasonable approximation of the real behavior of the pulse between two time steps. A piecewise-constant approach has also been tested and leads to almost the same results.

The step size of the coarse graining is indicated by the vertical dashed lines in the background of Fig. 3 (top). In particular, at the maxima and minima of the pulse, there will be a significant difference between the original and the coarse-grained pulse. As a result, the increase in the  $m_\ell$  expectation value is too slow, which results in a final fidelity of only 22% while the most populated state is  $|49\rangle$  (data not shown). Nevertheless, qualitatively the evolution is similar to the original one and it may be possible to attenuate the effect of coarse graining by increasing the amplitude in a well-adjusted way.

A more elegant way to solve this problem consists in shaping directly the two quadratures. This corresponds to an optimization in the rotating frame and is shown in Fig. 4 (top). It essentially circumvents the issue of limited time resolution altogether since the time dependence of the complex shape function  $S_{\text{RF}}(t)$  is sufficiently slow to be insensitive to the coarse graining. Thus, the fidelity decreases by only 0.06% compared to the original pulse without coarse graining. This is a striking improvement compared to the brute force approach and highlights once more the importance of choosing the proper frame of reference.

### B. Fluctuating field strengths

The second most important source of noise are fluctuations in the DC and RF fields. In theory, the DC field is assumed to be perfectly static, which is not the case in a real experiment. DC field fluctuations lead to an uncertainty in the position of the energy levels in the Stark manifold. To check the stability of the pulse with respect to this noise, we have calculated the Hamiltonian for DC field strengths of  $\mathcal{E}_{\text{DC}} \pm \Delta\mathcal{E}_{\text{DC}}/2$  with  $\Delta\mathcal{E}_{\text{DC}} = 50\text{ }\mu\text{V/cm}$  and  $150\text{ }\mu\text{V/cm}$ , corresponding to the best and worst case scenarios in a real experiment, respectively. Then, we have propagated the initial state under the action of each of these Hamiltonians and of the optimized two-step amplitude pulse. It turns out that, in both cases, the loss of fidelity with respect to the original DC field strength is of the order of  $10^{-4}$  only. The robustness of our optimized pulse can be understood as follows. An offset in the DC field leads to the accumulation of an erroneous phase. This phase is proportional to the DC field offset and the pulse duration. The high stability of the optimized pulse is thus a direct result of its short duration.

Next, we consider amplitude noise in the RF pulse. To investigate its influence, we simulate fluctuations by adding a white-noise stochastic contribution. The noisy amplitude  $\tilde{\mathcal{E}}_{\text{RF}}(t)$  is realized as

$$\tilde{\mathcal{E}}_{\text{RF}}(t) = (1 + R \cdot f_{\text{noise}})\mathcal{E}_{\text{RF}}(t), \quad (11)$$

where  $R \in [-1, 1]$  is a random number and  $f_{\text{noise}} \in [0, 1]$  is the noise strength. Note that the range of  $f_{\text{noise}}$  implies amplitude fluctuations of at most up to a factor of two with respect to the original pulse. To avoid discontinuities, the random number  $R$  is fixed for a half-period,

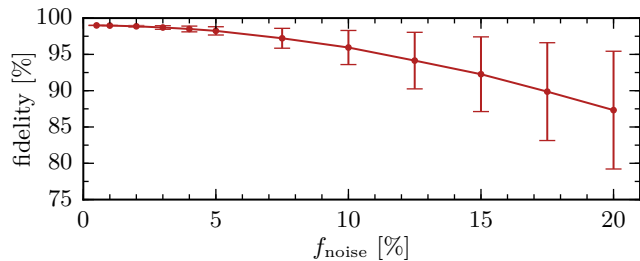


FIG. 5. Fidelity of the optimized pulse as a function of noise strength,  $f_{\text{noise}}$ . Shown are the averaged values from 1000 repetitions with randomly generated noise. The error bars indicate the standard deviation  $\sigma$ . The red line serves as a guide for the eye.

i.e. between two zeros of the pulse. In other words, we assume the fluctuations to occur on a time scale slower than half a period of the RF pulse ( $\sim 2$  ns). Moreover, the  $x$ - and  $y$ -component are modified independently such that we also account for polarisation noise in the simulation.

The impact of the RF amplitude noise on the fidelity of the target state is evaluated by repeating the propagation 1000 times, each with a different realization of Eq. (11), for noise strengths between 0.5% and 20%. As can be seen from Fig. 5, the fidelity decreases for higher noise strengths and the spread becomes larger. For example, a fidelity of 95.9% is expected on average for a noise level of 10%. This roughly corresponds to the present estimate of amplitude fluctuations in the experiment [2, 16], a value that could be reduced with simple experimental improvements. Even at a level of 10% amplitude noise, the optimized pulse leads to significantly faster and more accurate circularization than achieved with e.g. a  $\pi$ -pulse [2, 16].

## VI. QUANTUM SPEED LIMIT

Quantum mechanics itself sets a natural lower bound on the minimal time that is needed to realize a certain dynamics [32]. In the following, we will investigate the quantum speed limit for the circularization beyond (present) experimental constraints using optimal control theory. The speed limit has been investigated for multipartite systems such as entangling gates between atomic qubits [33] or transport in a spin chain [12]. In these cases, it is the interaction strength between the subsystems that sets the speed limit. Here, such a limit is absent. To the best of our knowledge, this is the first time that the speed limit for unary system dynamics in a realistic model is considered.

To speed up the circularization, we gradually increase the field strength of the guess pulse. In this context, it is important to keep in mind that our model consists of only the two lowest diagonal ladders. Eventually, this approximation will cease to be valid. We first discuss the

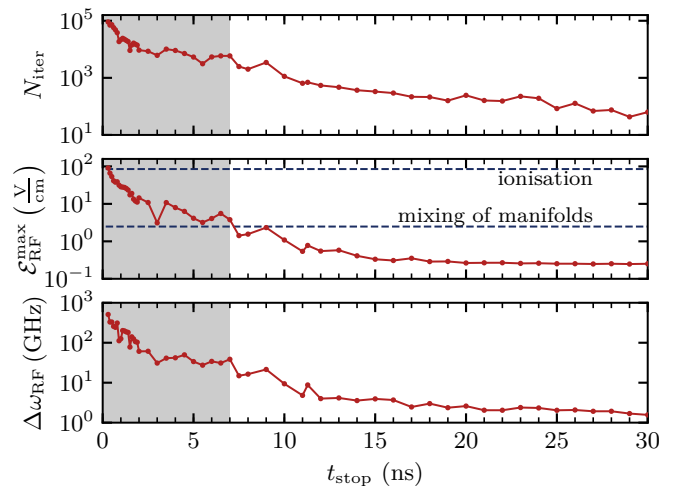


FIG. 6. Number of required iterations  $N_{\text{iter}}$  to reach a fidelity of  $J_T = 10^{-2}$  together with the required maximal field strength  $\mathcal{E}_{\text{RF}}^{\text{max}} = \max_t |\mathcal{E}_{\text{RF}}(t)|$  and bandwidth  $\Delta\omega_{\text{RF}}$  of the corresponding optimized pulse for different pulse lengths  $t_{\text{stop}}$ . The two field strengths where the adjacent manifolds start to mix with the central  $n$ -manifold and where the atom is ionized are marked by horizontal dashed lines. The grey background indicates the region where the model ceases to be predictive. The red lines serve as a guide for the eye.

QSL for our model and then examine the implications for the actual atom. No constraints on the optimized pulse are included except for Eq. (8). The optimization is performed until the functional crosses the threshold  $J_T = 10^{-2}$ . For each value of  $t_{\text{stop}}$ , we have tested several guess pulses with different edge times and field strengths. In Fig. 6, we have plotted the number of iterations required to reach the desired fidelity for the best guess, i.e., the pulse that needs the least number of iterations. It is evident from the figure that the number of iterations increases as the pulse becomes shorter. The fluctuations in the data points can be credited to the high sensitivity of the optimization to the guess pulse. In principle, Fig. 6 suggests that it is possible to circularize the atom within less than 1 ns. However, when the field strength of the optimized pulse increases dramatically, our model will cease to be predictive for the actual atomic system since we account for a small part of the Hilbert space only.

The first approximation is to neglect higher diagonal ladders in the  $n = 51$ -manifold. Because the transition frequencies between the pivotal states and the omitted states are larger and the dipole matrix elements smaller than between the states in the considered part of the Hamiltonian, a re-optimization to reach the desired fidelity is possible in principle. The optimized fields will certainly look different but the possibility of reaching the target state will not be affected. Nevertheless, the numerical calculations become rather demanding. One iteration of a pulse with  $t_{\text{stop}} = 7$  ns needs a computation time of about 6 s in our model (involving 101 states).



In contrast, when all states of the central  $n$ -manifold are considered ( $\sim 2500$  states), one iteration of the optimization requires approximately ten minutes. The total computation time is given by that estimate times the number of iterations, of the order of  $10^4$  for  $t_{\text{stop}} = 7$  ns, and increasing for decreasing  $t_{\text{stop}}$ .

The next approximation is omission of adjacent Stark manifolds. As the driving RF field becomes stronger, the states in the Stark manifold get increasingly dressed and the energy spacing increases. Once the dressing is strong enough to induce a crossing of adjacent manifolds, the instantaneous eigenenergies of our model will significantly differ from the ones obtained when considering the full atomic system. As a result, our model does not describe the actual atom any more. In the following, we will derive an approximation for the critical RF field strength where this effect becomes non-negligible.

For reasons of simplicity we will neglect the quantum defect here. Because the position of the centre of a manifold is given by the Rydberg formula (cf. Eq. (1)) the central  $n$ -manifold will cross the upper  $(n+1)$ -manifold first. Moreover, the eccentricity quantum number takes its maximal possible value of  $|\mu| = n-1$  at the top and the bottom of the  $m_\ell = 0$ -ladder, which results in the largest possible first-order Stark splitting (cf. Eq. (2) and Fig. 1). In addition, the energy levels get dressed by the RF field. The eigenstates of a perfect spin- $J$  system coupled to a field mode are separated in energy by the Rabi frequency  $\Omega = |\vec{\Omega}|$  (cf. Eq. (3)) [16]. When each pair of states acquires an additional energy splitting of  $\Omega$ , the edges of the diagonal spin ladder are shifted by  $\Omega(n-1)/2$  with respect to the middle of the ladder. Adding up all contributions and considering a resonant RF field, the position of states at the top (+) or bottom (−) of the  $m_\ell = 0$ -ladder is given by

$$E_n^\pm = -\frac{1}{2n^2} \pm \frac{3}{2}(n-1)n \mathcal{E}_{\text{DC}} \pm 3n \mathcal{E}_{\text{RF}} \frac{n-1}{2}. \quad (12)$$

Solving  $E_{51}^+ = E_{52}^-$  for  $\mathcal{E}_{\text{RF}}$  with  $\mathcal{E}_{\text{DC}} = 2.346$  V/cm results in a critical field strength of 2.5 V/cm for the driving field. This value is in agreement with the numerical calculation of the instantaneous eigenenergies of the  $n = 50$  to 52 manifolds for different RF field strengths when taking the quantum defect into account.

As a result, our model ceases to be predictive for RF field strengths above this value, which, according to Fig. 6, concerns all pulses that are shorter than approximately 7 ns. For these RF fields strengths, our model provides no longer an appropriate description of the Rydberg atom and it is not possible to draw any definite conclusion about the possibility to circularize the atom with sufficient confidence. While it may still be possible to reach the target circular state under these very strong and broad pulses, the numerical effort to check the hypothesis poses a serious obstacle. When considering the extended Hilbert space containing all states with  $n = 51 \pm 1$  and  $m_\ell \geq 0$  ( $\sim 4000$  states), the computation time of one iteration increases to one hour. Thus, the op-

timization becomes numerically infeasible because more than  $10^4$  iterations are necessary to provide the desired fidelity.

Eventually, when the field strength of the RF field is increased even further, a hard physical bound is reached when the fields are strong enough to ionise the atom. For states on the lowest diagonal ladder, the order of magnitude of the necessary field strength is given by the static field ionization threshold,  $\mathcal{E} = 1/(9n^4)$  [15], which is 83 V/cm for  $n = 51$ .

In summary, we find the speed limit to be determined by the internal structure of the atom. In other words, the speed limit is defined in terms of the spectrum of the field-free Hamiltonian [32] but for real physical systems, this Hamiltonian is typically an idealization. For very strong external control fields, this idealization ceases to be valid. It is thus important to keep the assumptions on which the Hamiltonian is based in mind when determining the quantum speed limit.

## VII. CONCLUSIONS

We have tackled the question of how to prepare a Rydberg atom both quickly and accurately in a circular state. The necessary angular momentum transfer is realized by a suitably-shaped RF pulse. Using quantum optimal control theory, we have shown that the circularization can be sped up by a factor of three to take merely 65 ns. Even more importantly, the fidelity can be boosted from about 80% to 99%. The pulse has been constructed such as to be compatible with the current experimental setup [2] in terms of maximal field amplitude and spectral bandwidth. We have found that the time needed for the circularization is mainly determined by the experimentally available RF field strength.

We have tested our optimized RF pulses for robustness against various sources of noise. Overall, we find the protocol to be surprisingly stable. This is due to the short duration and small bandwidth of the pulse. The most detrimental source of noise are amplitude fluctuations of the RF field. Fluctuations above about 5% are found to compromise the circularization fidelity. When considering improvements of the experimental setup, stabilization of the RF field amplitude should thus be a priority. The optimized pulse is currently being implemented in the experiment and the first results look very promising.

Key to the successful derivation of an experimentally feasible shaped RF pulse was the careful construction of a pre-optimized guess field, exploiting previous insight into the circularization dynamics. In fact, in quantum optimal control theory, many solutions to a given control problem can typically be found. Which of these solutions is obtained in numerical optimization is then determined by the guess with which the iterative algorithm is initialized. Starting with a  $\pi$ -pulse that approximately rotates the system state onto the North pole of the  $J = (n-1)/2$  spin Bloch sphere [2] results in optimized pulses that are

unnecessarily strong and spectrally broad.

In general, pre-optimization of the guess pulse is a worthwhile endeavor to guide the optimization towards experimentally feasible pulses. It can be carried out in a semi-automatic way by parametrizing the field and determining the best parameters before handing over to a gradient-based search [34]. In the case of circularization, a numerical pre-optimization of the guess pulse turned out not to be necessary. Analysis of the solution obtained by optimizing a  $\pi$ -pulse revealed that the dynamics can be split into the preparation of a SCS and a rotation, with the proper angle, of this SCS towards the North pole. While the rotation requires the largest possible field strength to proceed at maximum speed, the preparation of the SCS is hampered by a large field strength. The run-off of population to other levels during the preparation of the SCS explains why a simple  $\pi$ -pulse fails. An intuitive solution is thus to decrease the amplitude during the SCS preparation, while ramping it up for the rotation of the SCS. With such a guess field, the optimization has to introduce only small adjustments that do not come with an increase of bandwidth or amplitude.

Splitting the transfer to the circular state into two steps furthermore allows us to identify what limits the minimum time required for the circularization. The time scale for preparing a SCS is given by the detuning of the RF pulse from undesired transitions to states with lower angular momentum projection, whereas the time to rotate the SCS to the North pole is determined solely by the Rabi frequency. A further speed up would thus be possible by using (a) a larger DC field strength, which increases the detuning, and (b) a larger RF field strength, which allows for faster rotation.

For the given DC field strength, increasing the RF field strength could, in principle, bring the circularization time down to about 10 ns. However, this would come not only at the price of large RF amplitudes but also of a much broader spectral bandwidth. Therefore, given the present

experimental technology, circularization times much below 50 ns do not seem realistic.

Of course, it is still interesting to investigate, from a theoretical point of view, the fundamental limit to the minimum time for circularizing a Rydberg atom. Previously, the quantum speed limit has been discussed for multi-partite systems where the interaction strength is the key factor [12, 33], whereas here we have considered dynamics in a unary system. We have found that, using quantum optimal control theory, the duration of the circularization can be decreased by yet another order of magnitude while maintaining sufficient accuracy. However, the control fields become so strong that eventually the theoretical model ceases to be reliable.

Since any theoretical description of a physical system is always based on idealization and simplifying assumptions, this finding is not restricted to Rydberg atoms. In fact, in a unary system, it is the spectrum of the field-free Hamiltonian alone that determines the speed limit [32]. One could thus be led to think that it is possible to push the minimum duration for a certain dynamics to arbitrarily small values by using control fields that are strong enough to distort the spectrum. However, such strong fields will eventually always result in loss processes and thus introduce an effective speed limit. It would be interesting to rigorously account for this phenomenon in the fundamental theory of the quantum speed limit.

## ACKNOWLEDGMENTS

We thank E.-K. Dietsche and A. Larrouy for discussions. Financial support from the European Union under the Research and Innovation action project “RYSQ” (Project No. 640378) is gratefully acknowledged.

- 
- [1] R. G. Hulet and D. Kleppner, *Phys. Rev. Lett.* **51**, 1430 (1983).
  - [2] A. Signoles, E.-K. Dietsche, A. Facon, D. Grosso, S. Haroche, J.-M. Raimond, M. Brune, and S. Gleyzes, *Phys. Rev. Lett.* **118**, 253603 (2017).
  - [3] J. M. Raimond, M. Brune, and S. Haroche, *Rev. Mod. Phys.* **73**, 565 (2001).
  - [4] M. Brune, E. Hagley, J. Dreyer, X. Maître, A. Maali, C. Wunderlich, J. M. Raimond, and S. Haroche, *Phys. Rev. Lett.* **77**, 4887 (1996).
  - [5] D. Maxwell, D. J. Szwer, D. Paredes-Barato, H. Busche, J. D. Pritchard, A. Gauguier, M. P. A. Jones, and C. S. Adams, *Phys. Rev. A* **89**, 043827 (2014).
  - [6] A. Facon, E.-K. Dietsche, D. Grosso, S. Haroche, J.-M. Raimond, M. Brune, and S. Gleyzes, *Nature* **535**, 262 (2016).
  - [7] A. Ramos, K. Moore, and G. Raithel, *Phys. Rev. A* **96**, 032513 (2017).
  - [8] P. Nussenzveig, F. Bernardot, M. Brune, J. Hare, J. M. Raimond, S. Haroche, and W. Gawlik, *Phys. Rev. A* **48**, 3991 (1993).
  - [9] M. H. Goerz, E. J. Halperin, J. M. Aytac, C. P. Koch, and K. B. Whaley, *Phys. Rev. A* **90**, 032329 (2014).
  - [10] S. J. Glaser, U. Boscain, T. Calarco, C. P. Koch, W. Köckenberger, R. Kosloff, I. Kuprov, B. Luy, S. Schirmer, T. Schulte-Herbrüggen, D. Sugny, and F. K. Wilhelm, *Phys. Rev. Lett.* **114**, 279 (2015).
  - [11] H. Yuan, C. P. Koch, P. Salamon, and D. J. Tannor, *Phys. Rev. A* **85**, 033417 (2012).
  - [12] T. Caneva, M. Murphy, T. Calarco, R. Fazio, S. Montangero, V. Giovannetti, and G. E. Santoro, *Phys. Rev. Lett.* **103**, 240501 (2009).
  - [13] M. H. Goerz, F. Motzoi, K. B. Whaley, and C. P. Koch, *npj Quantum Inf.* **3**, 37 (2017).
  - [14] M. J. Seaton, *Rep. Prog. Phys.* **46**, 167 (1983).
  - [15] T. F. Gallagher, *Rydberg atoms*, Cambridge Monographs

- on Atomic, Molecular, and Chemical Physics (Cambridge University Press, Cambridge, 1994).
- [16] A. Signoles, *Manipulation cohérented d'états de Rydberg elliptique par dynamique Zénon quantique*, Ph.D. thesis, Université Pierre et Marie Curie - Paris VI, France (2014).
  - [17] V. D. Mur and V. S. Popov, *Laser Phys.* **3**, 462 (1993).
  - [18] R. J. Glauber, *Phys. Rev.* **131**, 2766 (1963).
  - [19] H. A. Bethe and E. E. Salpeter, *Quantum Mechanics of One- and Two-Electron Atoms* (Plenum Publishing Corporation, New York, 1977).
  - [20] B. V. Numerov, *Monthly Notices of the Royal Astronomical Society* **54**, 592 (1924).
  - [21] R. Kosloff, *Annu. Rev. Phys. Chem.* **45**, 145 (1994).
  - [22] "QDYN library," [www.qdyn-library.net](http://www.qdyn-library.net).
  - [23] D. M. Reich, M. Ndong, and C. P. Koch, *J. Chem. Phys.* **136**, 104103 (2012).
  - [24] J. P. Palao and R. Kosloff, *Phys. Rev. A* **68**, 062308 (2003).
  - [25] J. P. Palao, R. Kosloff, and C. P. Koch, *Phys. Rev. A* **77**, 063412 (2008).
  - [26] A. Konnov and V. Krotov, *Automation and Remote Control* **60**, 1427 (1999).
  - [27] J. Somló, V. A. Kazakovski, and D. J. Tannor, *Chem. Phys.* **172**, 85 (1993).
  - [28] S. E. Sklarz and D. J. Tannor, *Phys. Rev. A* **66**, 053619 (2002).
  - [29] C. Gollub, M. Kowalewski, and R. de Vivie-Riedle, *Phys. Rev. Lett.* **101**, 073002 (2008).
  - [30] M. Schröder and A. Brown, *New J. Phys.* **11**, 105031 (13pp) (2009).
  - [31] M. Lapert, R. Tehini, G. Turinici, and D. Sugny, *Phys. Rev. A* **79**, 063411 (2009).
  - [32] V. Giovannetti, S. Lloyd, and L. Maccone, *Phys. Rev. A* **67**, 052109 (2003).
  - [33] M. H. Goerz, T. Calarco, and C. P. Koch, *J. Phys. B* **44**, 154011 (2011).
  - [34] M. H. Goerz, K. B. Whaley, and C. P. Koch, *EPJ Quantum Technol.* **2**, 21 (2015).